Published in final edited form as:
Biochemistry. 2009 April 14; 48(14): 3186–3196. doi:10.1021/bi9001166.

STRUCTURAL INSIGHTS INTO SUBSTRATE BINDING AND STEREOSELECTIVITY OF *GIARDIA* FRUCTOSE-1,6-BISPHOSPHATE ALDOLASE*

Andrey Galkin[1], **Zhimin Li**[2], **Ling Li**[2], **Liudmila Kulakova**[1], **Lipika R. Pal**[1], **Debra Dunaway-Mariano**[2], and **Osnat Herzberg**[1,*]

[1] *W. M. Keck Laboratory for Structural Biology, Center for Advanced Research in Biotechnology, University of Maryland Biotechnology Institute, Rockville, Maryland* [2] *Department of Chemistry and Chemical Biology, University of New Mexico, Albuquerque, New Mexico*

Abstract

Giardia lamblia fructose-1,6-bisphosphate aldolase (FBPA)1 is a member of the Class II zinc-dependent aldolase family that catalyzes the cleavage of D-fructose-1,6-bisphosphate (FBP) into dihydroxyacetone phosphate (DHAP) and D-glyceraldehyde-3-phosphate (G3P). In addition to the active site zinc, the catalytic apparatus of FBPA employs an aspartic acid, Asp83 in the *G. lamblia* enzyme, which when replaced by an alanine residue renders the enzyme inactive. A comparison of the crystal structures of the D83A FBPA in complex with FBP and of the wild-type FBPA in the unbound state revealed a substrate induced conformational transition of loops in the vicinity of the active site and a shift in the location of Zn^{2+}. Upon FBP binding, the Zn^{2+} shifts up to 4.6 Å towards the catalytic Asp83, which brings the metal within coordination distance to the Asp83 carboxylate group. In addition, the structure of wild-type FBPA was determined in complex with the competitive inhibitor D-tagatose 1,6-bisphosphate (TBP), a FBP stereoisomer. In this structure, the zinc binds in a site close to that previously seen in the structure of FBPA in complex with phosphoglycolohydroxamate, an analog of the postulated DHAP ene-diolate intermediate. Together, the ensemble of structures suggests that the zinc mobility is necessary to orient the Asp83 side chain and to polarize the substrate for proton transfer from the FBP C(4) hydroxyl group to the Asp83 carboxyl group. In the absence of FBP, the alternative zinc position is too remote for coordinating the Asp83. We propose a modification of the catalytic mechanism that incorporates the novel features observed in the FBPA/FBP structure. The mechanism invokes coordination and co-planarity of the Zn^{2+} with the FBP's O-C(3)-C(4)-O concomitant with coordination of Asp83 carboxylic group. Catalysis is accompanied by movement of Zn^{2+} to a site co-planar with the O-C(2)-C(3)-O of the DHAP. *gl*FBPA exhibit strict substrate specificity towards FBP and does not cleave TBP. The active sites of FBPAs contain an aspartate residue equivalent to Asp255 of *gl*FBPA, whereas tagatose-1,6-bisphosphate aldolase contains an alanine in this position. We and others hypothesized that this aspartic acid is a likely determinant of FBP vs. TBP specificity. Replacement of Asp255 by an alanine resulted in an enzyme that possesses double specificity, now cleaving TBP (albeit with low efficacy; k_{cat}/K_m = 80 $M^{-1}s^{-1}$) while maintaining activity towards FBP at 50-fold lower catalytic efficacy

[1]The abbreviations used are: FBPA, fructose-1,6-bisphosphate aldolase; *gl*FBPA, *Giardia* FBPA; *ec*TBPA, *E. coli* tagatose-1,6-bisphosphate aldolase; *ec*FBPA, *E. coli* FBPA; PGH, phosphoglycolohydroxamate; FBP, D-fructose-1,6-bisphosphate; TBP, D-tagatose-1,6-bisphosphate; DHAP, dihydroxyacetone phosphate; G3P, D-glyceraldehyde 3-phosphate.

*Corresponding author: Osnat Herzberg, Center for Advanced Research in Biotechnology, 9600 Gudelsky Drive, Rockville MD 20850, Tel: 240-314-6245; Fax: 240-314-6255; E-mail: osnat@carb.nist.gov.

Protein Data Bank coordinates entry codes: 3GAK, 3GAY, 3GB6

compared with the wild type FBPA. The collection of structures and sequence analyses highlighted additional residues that may be involved in substrate discrimination.

Members of the aldolase family catalyze retroaldol/aldol reactions that result in C-C bond cleavage/formation. The best studied aldolase family member is the fructose-1,6-bisphosphate aldolase (FBPA). FBPA catalyzes the reversible cleavage of D-fructose-1,6-bisphosphate (FBP) to dihydroxyacetone phosphate (DHAP) and D-glyceraldehyde-3-phosphate (G3P) (EC 4.1.2.13; Fig. 1A), a key step of the classical Embden-Meyerhof-Parnas glycolytic pathway.

Two evolutionarily and mechanistically unrelated FBPA classes have been identified, class I (which employs an active site lysine in Schiff base formation) and class II (which employs a Zn^{2+} cofactor) (1,2). The crystal structures of the class II FBPA from *E. coli* (*ec*FBPA) in the apo state and in complex with the inhibitor phosphoglycolohydroxamate (PGH, Fig. 1C), have been elucidated (3–5). The class II FBPA adopts an $(\alpha/\beta)_8$-barrel fold. At the active site, the Zn^{2+} coordinates the imidazole groups of three histidine residues and the C(2)=O and N(3)OH oxygen atoms of the FGH inhibitor. The structure of the *E. coli* tagatose-1,6-bisphosphate aldolase (*ec*TBPA), a class II aldolase acting on D-tagatose-1,6-bisphosphate (TBP, the C(4) hydroxyl epimer of FBP, Fig. 1B), has also been reported in complex with PGH (6), and it revealed the same Zn^{2+} coordination pattern. The structural data, together with the kinetic behavior of active site site-directed mutants, led investigators to propose a model of the class II FBPA substrate recognition and catalysis in which the Zn^{2+} plays a central role (7–9).

Despite the growing knowledge of the structure and catalytic mechanism of the Zn^{2+}-dependent enzymes, the binding interactions that take place between enzyme, cofactor and substrate in the Michaelis complex are not fully known. Specifically, there is no structural information showing how the G3P product, or the intact hexose unit of the FBP substrate, bind to FBPA.

Giardia lamblia, a flagellated protozoan, is a disease-causing parasite in developing and developed countries. Giardiasis symptoms range from severe diarrhea, weight loss, vomiting and malnutrition and if not treated might lead to death. Giardiasis is often difficult to treat because of increasing drug resistance, recurrence, and undesirable side affects. Previously, we reported the crystal structure and kinetic characterization of FBPA from *Giardia lamblia* (*gl*FBPA) (10). We suggested that the enzyme is a potential target for the development of new drugs against giardiasis because it is essential for *Giardia* survival and because, unlike the human and other mammalian FBPAs that belong to the class I aldolase family (11), the *gl*FBPA belongs to the class II aldolases. Our goal is to define the determinants of catalysis and substrate specificity of *gl*FBPA and to discover inhibitors that serve as leads for drug development. In previous work we showed that *gl*FBPA does not cleave TBP, which is a competitive inhibitor of the enzyme (K_i = 1 μM), despite the higher sequence identity of *gl*FBPA with *ec*TBPA (38%) compared with *ec*FBPA (23%) (10). We also confirmed that replacement of a key catalytic aspartic acid residue (Asp83 in *gl*FBPA numbering) by alanine using site-directed mutagenesis eliminated enzyme activity. This information provides the framework for the current study, which compares the structure of the ligand-free enzyme with the structures of *gl*FBPA/TBP and the D83A *gl*FBPA/FBP complexes to obtain insight into substrate induced changes in active site structure and into the mechanisms of substrate recognition and activation.

Methods

Crystallization and data collection

Recombinant wild-type *gl*FBPA and the D83A and D255A *gl*FBPAs mutants were produced and purified as described previously (10). Electrospray ionization time-of-flight mass spectrometry was performed in the University of New Mexico facility, to show that the N-

terminal methionine is removed by posttranslational modification. Crystals were grown at room temperature in hanging drops using the vapor diffusion method. Orthorombic crystals were obtained from protein solution that was mixed with an equal volume of mother liquor containing 18–25% Polyethylene glycol 3350, and 0.2 M of NH_4NO_3. Hexagonal crystals of ligand-free enzyme were obtained from mother liquor containing 0.2 M $MgSO_4$. The hexagonal crystals diffracted X-rays to a resolution of 2.9 Å. Orthorhombic crystals of wild-type protein in complex with TBP were obtained from protein solutions that were incubated on ice for 20 min with 10 mM TBP prior crystallization. The crystals diffracted X-rays to a resolution of 1.8 Å. Orthorhombic crystals of D83A *gl*FBPA in complex with FBP were obtained from protein solutions that were incubated on ice for 20 min with 20 mM FBP prior to crystallization. The crystals diffracted X-rays to a resolution of 2.0 Å. All crystals required a period of 2–5 weeks to appear. For data collection, the crystals were transferred to solutions containing mother liquor and 20% glycerol, and flash-cooled in liquid nitrogen.

Diffraction data were acquired at 100 K using an RAXIS IV++ image plate detector mounted on a Rigaku MicroMax 007 rotating anode X-ray generator (Rigaku MSC Inc.). Data processing was carried out using the CrystalClear program, version 1.3.6 (Rigaku MSC Inc.). The statistics of data collection are provided in Table 1.

Structure determination and refinement

The crystal structures were determined by Molecular Replacement with the computer program Phaser (12), using the high resolution orthorhombic (space group $C222_1$) FBPA/PGH structure as the search model (PDB entry code 2ISW). When difference Fourier maps indicated alternative tracing, new segments were modeled manually using the program 'O' (13). Structure refinement was carried out using the CNS program (14). For the apo FBPA, refined at 2.9 Å resolution, only positional, and group B-factor refinement with a bulk solvent correction was performed, whereas individual B-factors were refined for the FBPA complexes determined at higher resolution. The two molecules in the asymmetric unit were refined independently. Water molecules were added to the model based on the F_o-F_c difference Fourier electron density map (where F_o and F_c are the observed and calculated structure factors, respectively), using peaks with density $\geq 3\sigma$ as the acceptance criteria. The final stages of refinement of the apo FBPA structure were performed with REFMAC (15). PROCHECK was used for analysis of geometry (16), QUANTA for molecular modeling and structural alignment (Molecular Simulations Inc.), and PYMOL for depiction of the structures (17).

Steady-state kinetic constant determination of D255A glFBPA

Initial velocities were measured at 25 °C using 1 mL reaction solutions containing *gl*FBPA (0.5 μM for monitoring FBP (Sigma) cleavage and 30 μM for monitoring TBP (a gift from Dr. Wolf-Dieter Fessner of TU Darmstadt, Germany) cleavage, 200 μM NADH (Sigma), 5 U triosephosphate isomerase (Sigma), 2 U glycerol-3-phosphate dehydrogenase (Sigma) and varying concentrations of FBP or TBP (0.5 K_m–10 K_m) in 50 mM K^+HEPES (pH 7.5). The absorbance of the reaction solution was monitored at 340 nm ($\varepsilon = 6.2\ mM^{-1}\ cm^{-1}$).

To determine the kinetic constants, the initial velocity data were fitted to Equation 1 with KinetAsystI (IntelliKinetics, PA).

$$V_0=V_{max}[S]/(K_m+[S]) \quad (1)$$

where [S] is the substrate concentration, V_0 is the initial velocity, V_{max} is the maximum velocity, and K_m is the Michaelis-Menten constant for the substrate. The k_{cat} value was calculated from

V_{max} and the enzyme concentration [E] (determined employing the Bradford method (18)) using the equation $k_{cat} = V_{max}/[E]$.

Sequence search and alignment

Sequence analysis was carried out against microbial genomes (containing 940 bacterial and 48 archeal genomes in NCBI) using BLAST(19) with inclusion E-value threshold of 1E-05. Sequence relatives of *gl*FBPA were aligned using MUSCLE (v.3.6) with its default parameters (20). Amino acid multiple sequence alignment displayed as logos diagrams was generated using the WebLogo program (http://weblogo.berkeley.edu/logo.cgi) (21).

Results and Discussion

Overall structure of glFBPA

The structure refinement statistics are summarized in Table 1, and electron density maps in the vicinity of the active site are shown in Fig. 2. All structures of the *gl*FBPA contain two tightly-packed protein molecules in the asymmetric unit corresponding to the biological unit. Each subunit (denoted A and B) folds into an $(\alpha/\beta)_8$ barrel as seen in structures of *gl*FBPA/PGH complex and in the structures of other bacterial class II aldolases (3–6,22).

Apo *gl*FBPA—The ligand-free *gl*FBPA crystals were fragile and very sensitive to manipulation. They diffracted only to a resolution of 2.9 Å and exhibited high mosaic spread (2.5°). Therefore no water molecules were assigned. The model contains 592 amino acid residues, four sulfate anions and two zinc cations. Superposition of the two *gl*FBPA subunits yields a root-mean-square deviation (rmsd) in α-carbon positions of 0.5 Å. No electron density is associated with the following surface residues: 138–152, 175–190 and 323–324 in molecule A; 138–152, 187–190 and 323–324 in molecule B. These residues were omitted from the final model. The active site of each subunit is occupied by one Zn^{2+} and two sulfate ions that are positioned 9 Å apart. The sulfate ions originated from the crystallization solution (0.2 M of $MgSO_4$) and they occupy the FBP/TBP phosphoryl sites. A similar result was obtained for the positions of two sulfate ions bound in the active site of apo FBPA from *Thermus aquaticus*, which was crystallized from solution containing ammonium sulfate (22). Because the positions and interactions of the sulfate ions in the ligand-free *gl*FBPA structure overlap with those of the phosphoryl groups of the FBP and TBP ligands, the detailed description of the interactions will be discussed in the section describing these ligands.

Each subunit contains a Zn^{2+} cofactor (Fig. 2 A&B). In molecule A, Zn^{2+} coordinates the Glu135 carboxyl group and His210, and is located 3.2 Å away from His84 (too long a distance for direct coordination) (Table 2). The loop comprising residues 176–187 and containing the active site His178, is disordered. In molecule B, Zn^{2+} coordinates all three histidine residues His84, His210 and His178.

(b) The FBPA/TBP complex—The model includes 637 amino acid residues and 578 water molecules. Each active site is occupied by a TBP ligand (Fig. 2C). Pair wise superposition of two monomers results in rmsd between α-carbon positions of 0.3 Å. No electron density is associated with the surface residues 144–146 in molecule A and residues 144–147 in molecule B. These residues were omitted from the final model.

(c) The D83A FBPA/FBP complex—The model includes 635 amino acid residues and 569 water molecules. Each active site is occupied by a FBP ligand and a Zn^{2+} ion, which binds in two mutually exclusive sites, each with half occupancy (Fig. 2D). Pair wise superposition of the two monomers results in rmsd between α-carbon positions of 0.3 Å. No electron density is

associated with residues 144–147 in molecule A and residues 144–148 in molecule B. These residues were omitted from the final model.

Structural changes upon ligand binding

Pair wise superposition of both molecules of the apo and ligand-bound *gl*FBPA shows local changes in loop regions (Fig. 3). These loops are located remotely from crystal contacts and thus the differences are attributed solely to ligand binding. The most striking response to both FBP and TBP binding is the ordering of the loops spanning residues 135–155 and residues 174–194, which are largely disordered in the ligand-free FBPA structure. The 174–194 loop caps the ligand C(4)-C(6) whereas the 135–155 loop tucks in the 174–194 loop and four of its residues that do not contact the 174–194 loop remain disordered (144–147). Upon ligand binding, Lys182 and His178 located on the 174–194 loop form key interactions with FBP/TBP and the Zn^{2+} (Figs. 2&4). A third loop, encompassing residues 227–237, undergoes substantial rearrangement, with the Ala233 and Val234 Cα atom positions in the middle of the loop shifting by 2.7 Å from their positions in the ligand-free structure in order to accommodate the 174–194 loop (Fig. 3).

Substrate binding site

To obtain detailed molecular insights into catalysis and substrate recognition, we determined the crystal structure of the wild type *gl*FBPA in complex with the FBP C(4) hydroxyl epimer, TBP, which is a competitive inhibitor of the enzyme, and that of the *gl*FBPA D83A mutant in complex with the substrate FBP (Fig. 4). The two crystals are isomorphous and the D83A mutation does not alter the overall fold as evidenced by the superposition of the two structures that yields an rmsd between Cα traces of 0.3 Å. It is clear from the electron density maps that both ligands bind in the acyclic keto form of their respective hexoses (Fig. 2 C&D), although it has been reported that in solution FBP exists mainly (*ca*. 98%) in the cyclic hemiketol form (23). Indeed, the active site is a rather narrow crevice designed to accommodate an acyclic substrate. The K_i = 1 μM of the tagatose inhibitor, when adjusted to reflect the population of the acyclic form defines a remarkably low K_d = 20 nM.

As evident from the *gl*FBPA/FBP complex, the two ends of the substrate are pinned into place *via* interactions of electropositive residues with the C(1) and C(6) phosphate groups (Fig 4A). The conformation of the substrate at the reaction center (*viz*. the C(3)–C(4) bond) is further defined through hydrogen bond formation between the Gly211 NH and Asp255 carboxylate group with the C(2)=O and C(5)OH, respectively. Finally, the C(3)OH is anchored by its interaction with Gln48 and Asn253 side chains and the Zn^{2+}, whereas the C(4)OH is anchored by its interactions with the Zn^{2+}. As discussed later, modeling that restores Asp83 instead of the alanine mutant shows that the C(4)OH also interacts with the Asp83 carboxylate group (Fig. 5).

In the following discussion, the *gl*FBPA active site is divided into three subsites; the DHAP binding site, the G3P binding site and the Zn^{2+} binding site.

(a) The DHAP site—The enzyme interactions with the FBP C(1)–C(3) moiety deviate from the interactions observed with the PGH inhibitor (10), whereas the enzyme interactions with the TBP C(1)–C(3) moiety do not. The FBP/TBP C(1)–C(3) moiety binds in a deep polar cavity with the C(1) dianionic phosphate group stationed in a site enriched with positive dipoles of backbone amide groups (Gly179, Ser213, Asp255 and Ser256) (Fig. 4). In addition, the C(1) phosphate interacts with the amino group of Lys182 on the 174–194 flexible loop and with the hydroxyl groups of Ser213 and Ser256. Unlike the PGH C(2)O, which forms a hydrogen bond with the Gly211 backbone amide group concomitantly with coordinating to the Zn^{2+}, the FBP C(2)=O interacts only with the backbone amide group of Gly211. In contrast to FBP, the C

(2)=O of the TBP exhibits the same two interactions as those of the PGH. The C(3)-OH of FBP, TBP, and the N-OH of PGH, are all coordinated to the Zn^{2+}, and they also form hydrogen bonds with the side chain amide groups of Asn253 and Gln48.

(b) The G3P site—The C(6) phosphate groups of both FBP and TBP interact with the Arg259 guanidinium group and that of Arg280 of the partner subunit (Arg331 in *ec*FBPA) (Fig. 4). The latter interaction is consistent with previous site directed mutagenesis results: Arg331 is essential for the C(6) phosphate group binding as evidenced by the R331A and R331Q *ec*FBPA mutants for which the K_m values for FBP are dramatically increased whereas the K_m for DHAP are unchanged (24). Both Arg259 and Arg280 of *gl*FBPA participate in an exquisite charge network that anchors them for optimal interaction with the ligand. Asp255 and Asp278 of the partner subunit interact with Arg259, and in turn Asp278 interacts with Arg280. Ser50, conserved in class II FBPAs (Ser61 in *ec*FBPA), forms a hydrogen bond with the C(6) phosphate group. Again, site directed mutagenesis experiments with the *ec*FBPA demonstrated the importance of this interaction. Firstly, the catalytic efficiency of the S61A FBPA is significantly lower (increased K_m and decreased k_{cat}) than that of the wild-type enzyme and secondly, whereas the wild-type enzyme exhibited G3P product inhibition, the S61A mutant did not (8).

(c) A shifting Zn^{2+} site—The electron density maps of all *gl*FBPA structures revealed a metal bound in the active site. Previously we used tunable synchrotron X-rays to show a peak at 9674.2 eV corresponding to the absorption edge of Zn (10). No zinc was added during protein purification and crystallization, which indicates high enzyme affinity to the Zn^{2+}. The same protein purification protocol was employed in the current studies. Also, the metal-ligand coordination distances are ~2.0–2.3 Å, and the metal coordinates histidine side chains, which is typical of Zn^{2+} (Table 2). Taken together, the evidence supports Zn^{2+} as the intrinsic metal bound in the active site.

One of the striking structural features of the Class II Zn^{2+}-dependent FBPAs is the promiscuity of the Zn^{2+} sites, coordination geometry and ligands. Analysis of zinc geometry in protein structures refined at resolution higher than 2 Å showed that the Zn^{2+} coordination distance to oxygen atoms is 2.3 ± 0.3 Å and to nitrogen atoms 2.1 ± 0.2 Å (25). As can be seen by viewing the data in Table 2, the Zn^{2+} coordination distances in *gl*FBPA are sometimes outside this range. We bracket potential ligands, which are located over 3 Å away from the metal to indicate weak interactions but nevertheless included them to contrast the different structures.

Previously three Zn^{2+} containing structures of *ec*FBPA, two ligand-free structures and one *ec*FBPA/PGH complex, were described (3–5). One of the ligand-free structures (PDB entry code 1zen) contains two Zn^{2+} ions, each exhibiting a coordination geometry described as distorted tetrahedral (4). We assigned these sites as Zn1 and Zn3 (Table 2). Another independently determined apo structure (pdb:1dos, (3)) revealed two mutually exclusive Zn^{2+} sites with approximately one half occupancy each. One site, corresponding to the Zn1 site that was described by Cooper and colleagues (4), and the second site, which we assign as Zn2 (Table 2), is not present in the 1zen PDB entry. The structure of the *ec*FBPA/PGH complex (5) exhibits two Zn^{2+} binding sites in each subunit (Zn2 and Zn4, Table 2). The authors proposed that Zn2 plays a catalytic role because it coordinates to the PGH O-C(2)-N(3)-O moiety. The zinc at the Zn4 site on the other hand was suggested to play a structural role. The new *gl*FBPA structures reported here reveal further diversity in Zn^{2+} binding.

Difference Fourier electron density maps (Fig. 2 A&B) show bound Zn^{2+} in both molecules of the crystal asymmetric unit of the apo *gl*FBPA, corresponding to Zn1 (in molecule A) and Zn2 (in molecule B). In molecule A, Zn^{2+} coordinates the side chains of His210 and Glu135 (Fig. 2A). His84 is oriented towards the metal but the distance is too great for direct

coordination (3.2 Å). In molecule B, Zn^{2+} coordinates three histidine residues His84, His210 and His178 (Fig. 2B). Because of the limited resolution of the diffraction data (2.9 Å), no water molecules could be assigned in the electron density map and therefore water ligands that might complete the Zn^{2+} coordination sphere elude detection.

In the *gl*FBPA/TBP complex, the Zn^{2+} is bound at the Zn2 site. The Zn^{2+} exhibits a trigonal bipyramidal coordination geometry that is similar but not identical to that seen in both *gl*FBPA and *ec*FBPA in complex with PGH, and it is located in the Zn2 site. Three Zn^{2+} ligands are provided by histidine residues; the N^{ε} nitrogen atoms of His84 and His178, and the N^{δ} atom of His210 (Fig. 2C). The TBP contributes C(2)O and C(3)O ligands, analogous to the C(2)O and N(3)O of the PGH ligand. However, the TBP C(2)O and C(3)O distances to the zinc (2.9 and 2.6 Å) are somewhat longer than the mean value reported by Wodak and colleagues (25). The elongated coordination bonds serve to avoid a clash between the TBP C(4) hydroxyl and the imidazole group of His178 (Fig. 4). Unlike the O-C(2)-N(3)-O of the PGH ligand, the O-C(2)-C(3)-O atoms of the TBP ligands are not co-planar with the Zn^{2+}.

For the *gl*FBPA D83A/FBP complex, the difference Fourier map (Fig. 2D) showed electron density for both molecules in the asymmetric unit, consistent with two mutually exclusive Zn^{2+} ions, 1.4 Å apart and with one half occupancy each (termed Zn2A and Zn2B in Table 2). Observations of mutually exclusive metal sites in FBPA have been reported. Specifically, dual metal binding occurs in one of the four protein molecules in the asymmetric unit of the class II *Thermus aquaticus* FBPA apo structure, where two mutually exclusive cobalt ions (2.5 Å apart) were modeled (22). In addition, in the *ec*FBPA apo structure (PDB entry 1dos) there are also two mutually exclusive Zn^{2+} ion binding sites, 3.2 Å apart; each of these sites is associated with alternate conformations of the two coordinated histidine residues, His10 and His264 (Table 2). Both alternate zinc sites of the *gl*FBPA D83A/FBP complex exhibit highly perturbed pentagonal geometry with long distances to the potential histidine ligands (in contrast to the short distances to the histidine residues in the PGH and TBP complexes) and typical oxygen coordination distances (2.1–2.2 Å) to the FBP C(3) and C(4) hydroxyl groups (Table 2). The location of the Zn2A site is close to that of Zn2 in the PGH/TBP inhibited-enzyme (1.0/0.9 Å apart, respectively). The Zn2B site is located 2.3 Å away from the Zn2 site and is unique because it is the only metal site observed in the collection of FBPA structures that allows coordination of the Asp83 (missing in the inactive D83A mutant but modeling the Asp83 based on all other *gl*FBPA structures suggests a ~2.2 Å coordination distance, Fig. 5). Notably, the O-C(3)-C(4)-O of the FBP ligand and the Zn2B are co-planar. The Ala83-His84 peptide bond in the *gl*FBPA D83A/FBP complex adopts an α-helical conformation ($\phi,\psi = -61,-36$) whereas it adopts a β-conformation in the *gl*FBPA/TBP complex ($\phi,\psi = -88,138$). Inspection of the two structures suggests that the conformational change may be attributed to the affect of the mutation; the Asp83 side chain orientation as seen in all wild-type FBPA structures ($\chi 1 = 180°$) results in steric clash with an ensuing helical peptide carbonyl group as seen in the D83A mutant enzyme, and the backbone CO of the mutated enzyme forms a hydrogen bond with an internal water molecule that is otherwise provided by Asp83 in the wild-type enzyme. In our discussion of the role of Zn2B in catalysis, which follows, we assume that the wild-type FBPA Asp83-His84 peptide maintains the β-conformation.

Catalytic mechanism - implication of the new structures

We suggest for consideration and future experimental exploration, a modification to the Class II aldolase catalytic mechanism proposed earlier based on PGH bound *ec*FBPA *ec*TBPA structures, which incorporates the insights provided by the liganded *gl*FBPA structures (Fig. 6). Based on the structures of the *ec*FBPA, Hunter, Berry and colleagues proposed that Asp109 (Asp83 in *gl*FBPA) abstracts a proton from the FBP C(4)OH in the C(3)–C(4) bond cleavage step, which leads to the ene-diolate intermediate, and that Glu182 (Glu143 in *gl*FBPA)

protonates the ene-diolate at C(3) in the ensuing step (5,9). The structures of *gl*FBPA in complex with either FBP or TBP reveal for the first time the identities of substrate binding residues and the catalytic residues "in total". Thus, in the presence of FBP and TBP, the flexible 138–152 loop adopts a conformation that places Glu143 carboxylate group 23 Å away from the C(3) of the FBP/TBP. In the complex with the PGH (the analog of the ene-diolate intermediate), residues 140–149 are disordered and Glu143 is undefined. Nevertheless, it is clear from the rest of the structure that the Glu143 carboxylic group is unlikely to reach the C (3) position and therefore its carboxylate group may not play the role of general acid. This conclusion is also consistent with the reported finding that the *ec*FBPA E182A mutant exhibits only a 37-fold reduction in catalytic efficiency (9). The *gl*FBPA/FBP structure indicates that when Asp83 is modeled into position (by analogy to its position in the PGH- or TBP-bound enzymes), the side chain is located 3.3 Å from the C(4) hydroxyl and 3.4 Å from the C(3) of FBP. We propose a step-wise mechanism in which Asp83 serves as both general base and general acid because it is poised appropriately for accepting the proton from the C(4)OH and, as the conjugate acid, delivering it to the C(3) of the putative ene-diolate intermediate.

The second finding from the *gl*FBPA/FBP structure, and in particular the Zn2B site, is that upon migration to this site the Zn^{2+} is positioned to orient and polarize the FBP C(4)OH, and simultaneously orient the side chain of Asp83, for proton transfer from the C(4)OH to Asp83 carboxylate group. Thus, the Zn^{2+} is an active participant in catalysis of C(4)OH deprotonation. The Zn^{2+} is also positioned to assist in the polarization of the FBP C(4)-C(3) bond. Specifically, Zn^{2+} coordination to C(3)OH coupled with the hydrogen bonds donated by Gln48 and Asn253 side chains serve to augment the Gly211 backbone amide interaction with the C(2)=O in stabilization of the transition state leading to the ene-diolate intermediate depicted in Figure 6.

The most intriguing feature of the Zn^{2+} cofactor is that it can migrate 4.6 Å from the Zn1 site to the Zn2B site, and that its coordination changes along the way (Fig. 5). The plasticity of Zn^{2+} coordination may be an important factor in catalysis. Ideally, Zn^{2+} coordination to the FBP C(3)O and C(4)O would be maximal at the first transition state and not at the ground state. The in-plane and out-of-plane Zn^{2+} coordination revealed by the three structures suggests mobility of the Zn^{2+} that might allow it to maximize coordination with the C(3)O coordination as the C(4) changes hybridization state in formation of the first transition state. Furthermore, the reduction in the strength of the Zn^{2+}coordination bond with the Asp83 upon protonation might drive the reorganization of the Zn^{2+} inner coordination sphere and the movement of Zn^{2+} to coordinate with the C(2)O and C(3)O of the ene-diolate intermediate may guide the Asp83 conjugate acid for proton delivery. At this stage, the ene-diolate C(3) becomes the obvious candidate for accepting the proton. In future work the model of catalysis inferred from the structures will be tested by site directed mutagenesis coupled with kinetic and structural analysis of the mutants.

Substrate specificity

Intriguingly, whereas both the amino acid sequence and crystal structure of *gl*FBPA are more similar to *ec*TBPA than to *ec*FBPA (38% and 23% sequence identity, respectively), the kinetic characterization showed unequivocally that the true substrate is FBP (10). Moreover, in contrast to *ec*FBPA, *gl*FBPA recognizes TBP as a tight binding inhibitor rather than as a substrate (10). We have now shown that as with the substrate FBP, TBP binds to the *gl*FBPA active site in the acyclic ketone form, however because of the difference in the stereochemistry at C(4), the C(4)OH of the TBP ligand is not coordinated by the Zn^{2+} nor is it positioned for proton abstraction by the putative general base Asp83 (Fig. 4). On the other hand, all other binding interactions remain unchanged, thus accounting for tight TBP binding without catalytic turnover. In order for the C(4)OH of the TBP ligand to assume the position of the C(4)OH of

the FBP ligand, rotation about the C(3)–C(4) bond must occur. Such rotation is expected to disrupt the favorable interaction between the C(5)OH and Asp255 and possibly the interaction of the C(6) phosphate group with Arg259, Arg280* (of the partner subunit) and Ser50 (Fig. 4).

The *gl*FBPA Asp83 counterpart in *ec*TBPA, Asp82, occupies the same position in the *ec*TBPA active site as Asp83 does in the *gl*FBPA active site (10) and Asp109 in *ec*FBPA (6). Thus, we anticipate that during catalysis, the respective C(4)OH groups are co-located, whereas the respective C(5)OH and C(6) phosphate groups are not. Perhaps it is no coincidence that *ec*TBPA does not conserve an aspartate at the site defined by Asp255 of the *gl*FBPA (Asp288 of *ec*FBPA and Ala232 of the *ec*TBPA) as the C(5)OH will not be properly positioned for hydrogen bond formation with this residue (i.e., assuming that the C(4)OH must be oriented to form the same interactions with the catalytic aspartate and the Zn^{2+}). To test this hypothesis, we replaced Asp255 of the *gl*FBPA by Ala so that its interaction with the TBP C(5)OH is eliminated, which in turn might allow a TBP C(4)–C(3) bond rotation. The D255A glFBPA was expressed, purified and characterized using steady-state kinetics (Table 3) showing that the mutant enzyme cleaves TBP (albeit with low efficacy, $k_{cat}/K_m = 80\ M^{-1}s^{-1}$) while losing 50-fold catalytic efficacy towards FBP. Interestingly, the K_m values of the mutant enzyme towards FBP and TBP are similar and they are 10–20 times higher than the FBP K_m of the wild-type enzyme. Earlier, Zgiby *et al*. reported that the *ec*FBPA D288A mutant did not display enhanced TBPA activity (8). Because the *gl*FBPA structure resembles that of the *ec*TBPA more closely than that of *ec*FBPA it may be more tolerant of the Ala for Asp replacement.

Potential sequence signatures of FBP vs. TBP selectivity

The close sequence identity (38%) between the *gl*FBPA and the *ec*TBPA may account for the ability to introduce the new activity by a single residue mutation. While the *gl*FBPA D255A mutation introduces new activity towards TBP, the single replacement does not fully switch stereospecificity. This is not surprising because the 38% sequence identity between *gl*FBPA and *ec*TBPA means that 62% of the residues are different, providing ample opportunity for additional built-in specificity determinants. For the purpose of identifying other important substrate discrimination determinants, we have analyzed the FBPA/TBPA sequence family using BLAST (19). The sequence search of the microbial genomes database resulted in 513 hits. Of these, 301 sequences contained an aspartic acid residue in the position corresponding to the *gl*FBPA Asp255, and 60 sequences contained alanine in this position. The remaining sequences contained residues other than aspartate or alanine in the 255 position and were excluded from further analysis. The annotations of most remaining sequences were consistent with the FBPA and TBPA division, however some sequences were annotated as FBPA/TBPA enzymes. To assure “clean” grouping, the sequences with dual activity annotation were removed from the analysis even though the basis for the annotation is not provided in the sequence database, leaving 289 sequences in the FBPA group and 51 sequences in the TBPA group.

Having produced two subfamilies based on the Asp/Ala 255 position, we then examined residue preferences in other sequence positions. Although the key residues involved in substrate interactions tend to be conserved in both groups, there are several clusters in the alignment that may comprise FBP/TBP specificity signature, especially in residues located in the 1st shell surrounding the ligand (defined by a distance between any ligand atom to a 1st shell residue that is shorter than 4 Å) and the 2nd shell residues (defined by distances between any residue to a 1st shell residue that are shorter than 4 Å) (Fig. 7).

The first stereospecificity signature sequence comprises residues 48–53 (*gl*FBPA numbering). In this region, Gln48 and Ser50 of the FBPA group (Fig. 7A) are 1st shell residues. In the *gl*FBPA structures, Gln48 NH_2 interacts with the C(3)OH of the FBP and TBP (3.2–3.5 Å)

(Fig. 4). Replacement by an alanine (the highest frequency residue in the TBPA group) makes the environment less crowded and provides more flexibility that may help with TBP accommodation in a productive binding mode. Ser50 interacts with the C(6) phosphoryl group of both ligands (Fig. 4). The threonine in this position is characteristic of the TBPA subfamily and it forms a hydrogen bond with another TBPA conserved threonine residue in position 53 – a 2nd shell residue (Ala in *gl*FBPA). The Pro in position 51, also a 2nd shell residue, is a hallmark of the "TBPA" subgroup. This residue, together with the replacement of Arg259 (a C(6) phosphoryl interacting residue) by a Lys in the TBPA subfamily may modify the phosphate binding site slightly in a manner more suitable for productive accommodation of TBP. Moreover, Arg259 forms an ion pair with Asp255. The alternative Lys-Ala pair, as found in the TBPA subfamily, leads to a less crowded phosphoryl environment that may facilitate the adjustment of the TBP in the active site.

Another interesting cluster of residues is found around His210 (Fig. 7C), a Zn^{2+} interacting residue (Fig. 4). Four residues preceding this histidine (PLVL) are invariant in the TBPA subfamily, whereas only a valine in position 208 is conserved in the "FBPA" sequences. This segment is outside the 1st and 2nd shells and perhaps contributes to stereo selectivity by fine tuning the positioning of the Zn^{2+}ion and its coordination properties.

In an earlier attempt to understand the substrate specificity of class II FBP/TBP aldolases, nine residues of the *ec*FBPA were identified as potentially impacting substrate discrimination and were mutated into the corresponding residues of *ec*TBPA (8). None of the mutations produced an enzyme with increased activity towards TBP, whereas many of them impaired FBPA activity. In another study, three rounds of *ec*TBPA directed evolution by DNA shuffling produced an enzyme that showed nearly 80-fold improvement in k_{cat}/K_m towards the non-natural substrate FBP (26). None of these evolved residues lie within the 1st shell binding site envelope. Two replacements altered the enzyme stereochemistry (equivalent to *gl*FBPA position 26 and 279). Inspection of their structural context suggest that they might have perturbed the position of the conserved arginine residue involved in C(6) phosphoryl binding (*gl*FBPA Arg280, Fig. 4). Two other evolved sequence positions correspond to residues invariant in both the TBPA and FBPA groups (Asp105 and Ser107 in *gl*FBPA). The side chains of these residues form a hydrogen bond network with His84, a Zn^{2+} ligands (Fig. 4). Berry and coworkers suggested that the replacement of these residues into glycines changed the orientation of the substrate, leading to altered stereochemistry. Asp105 and Ser107 are 2nd and 3rd shell residues.

Taken together, our results and those from earlier studies underscore the complexity of defining substrate stereospecificity, which involve amino acid residues within the 1st, 2nd and higher level shells surrounding the ligand. Moreover, there may be multiple routes for optimization of stereospecificity. Better insight into this fascinating issue will be gained from the structure of a TBPA/substrate complex.

Acknowledgements

Grant Sponsor: National Institute of Health RO1 AI059733.

We thank John Moult for insightful discussions and Patrick Mariano for critical reading of the manuscript.

References

1. Kobes RD, Simpson RT, Vallee RL, Rutter WJ. A functional role of metal ions in a class II aldolase. Biochemistry 1969;8:585–588. [PubMed: 5793710]
2. Rutter WJ. Evolution of Aldolase. Fed Proc 1964;23:1248–1257. [PubMed: 14236133]

3. Blom NS, Tetreault S, Coulombe R, Sygusch J. Novel active site in Escherichia coli fructose 1,6-bisphosphate aldolase. Nat Struct Biol 1996;3:856–862. [PubMed: 8836102]
4. Cooper SJ, Leonard GA, McSweeney SM, Thompson AW, Naismith JH, Qamar S, Plater A, Berry A, Hunter WN. The crystal structure of a class II fructose-1,6-bisphosphate aldolase shows a novel binuclear metal-binding active site embedded in a familiar fold. Structure 1996;4:1303–1315. [PubMed: 8939754]
5. Hall DR, Leonard GA, Reed CD, Watt CI, Berry A, Hunter WN. The crystal structure of Escherichia coli class II fructose-1, 6-bisphosphate aldolase in complex with phosphoglycolohydroxamate reveals details of mechanism and specificity. J Mol Biol 1999;287:383–394. [PubMed: 10080900]
6. Hall DR, Bond CS, Leonard GA, Watt CI, Berry A, Hunter WN. Structure of tagatose-1,6-bisphosphate aldolase. Insight into chiral discrimination, mechanism, and specificity of class II aldolases. The Journal of biological chemistry 2002;277:22018–22024. [PubMed: 11940603]
7. Plater AR, Zgiby SM, Thomson GJ, Qamar S, Wharton CW, Berry A. Conserved residues in the mechanism of the E. coli Class II FBP-aldolase. J Mol Biol 1999;285:843–855. [PubMed: 9878448]
8. Zgiby SM, Thomson GJ, Qamar S, Berry A. Exploring substrate binding and discrimination in fructose1, 6-bisphosphate and tagatose 1,6-bisphosphate aldolases. Eur J Biochem 2000;267:1858–1868. [PubMed: 10712619]
9. Zgiby S, Plater AR, Bates MA, Thomson GJ, Berry A. A functional role for a flexible loop containing Glu182 in the class II fructose-1,6-bisphosphate aldolase from Escherichia coli. J Mol Biol 2002;315:131–140. [PubMed: 11779234]
10. Galkin A, Kulakova L, Melamud E, Li L, Wu C, Mariano P, Dunaway-Mariano D, Nash TE, Herzberg O. Characterization, kinetics, and crystal structures of fructose-1,6-bisphosphate aldolase from the human parasite, Giardia lamblia. J Biol Chem 2007;282:4859–4867. [PubMed: 17166851]
11. Henze K, Morrison HG, Sogin ML, Muller M. Sequence and phylogenetic position of a class II aldolase gene in the amitochondriate protist, Giardia lamblia. Gene 1998;222:163–168. [PubMed: 9831644]
12. McCoy AJ, Grosse-Kunstleve RW, Storoni LC, Read RJ. Likelihood-enhanced fast translation functions. Acta Crystallogr D Biol Crystallogr 2005;61:458–464. [PubMed: 15805601]
13. Jones TA. Interactive electron-density map interpretation: from INTER to O. Acta crystallographica 2004;60:2115–2125.
14. Brünger AT, Adams PD, Clore GM, DeLano WL, Gros P, Grosse-Kunstleve RW, Jiang JS, Kuszewski J, Nilges M, Pannu NS, Read RJ, Rice LM, Simonson T, Warren GL. Crystallography & NMR system: A new software suite for macromolecular structure determination. Acta crystallographica 1998;54:905–921.
15. Murshudov GN, Vagin AA, Dodson EJ. Refinement of macromolecular structures by the maximum-likelihood method. Acta Crystallogr D Biol Crystallogr 1997;53:240–255. [PubMed: 15299926]
16. Laskowski RA, MacArthur MW. PROCHECK: a program to check the stereochemical quality of protein structures. J Appl Crystallogr 1993;26:283–291.
17. DeLano, WL. The PyMOL User's Manual. DeLano Scientific; San Carlos, CA, USA: 2002.
18. Bradford MM. A rapid and sensitive method for the quantitation of microgram quantities of protein utilizing the principle of protein-dye binding. Analytical biochemistry 1976;72:248–254. [PubMed: 942051]
19. Altschul SF, Madden TL, Schaffer AA, Zhang J, Zhang Z, Miller W, Lipman DJ. Gapped BLAST and PSI-BLAST: a new generation of protein database search programs. Nucleic acids research 1997;25:3389–3402. [PubMed: 9254694]
20. Edgar RC. MUSCLE: multiple sequence alignment with high accuracy and high throughput. Nucleic Acids Res 2004;32:1792–1797. [PubMed: 15034147]
21. Crooks GE, Hon G, Chandonia JM, Brenner SE. WebLogo: a sequence logo generator. Genome Res 2004;14:1188–1190. [PubMed: 15173120]
22. Izard T, Sygusch J. Induced fit movements and metal cofactor selectivity of class II aldolases: structure of Thermus aquaticus fructose-1,6-bisphosphate aldolase. The Journal of biological chemistry 2004;279:11825–11833. [PubMed: 14699122]
23. Midelfort CF, Gupta RK, Rose IA. Fructose 1,6-bisphosphate: isomeric composition, kinetics, and substrate specificity for the aldolases. Biochemistry 1976;15:2178–2185. [PubMed: 776219]

24. Qamar S, Marsh K, Berry A. Identification of arginine 331 as an important active site residue in the class II fructose-1,6-bisphosphate aldolase of Escherichia coli. Protein Sci 1996;5:154–161. [PubMed: 8771208]

25. Alberts IL, Nadassy K, Wodak SJ. Analysis of zinc binding sites in protein crystal structures. Protein Sci 1998;7:1700–1716. [PubMed: 10082367]

26. Williams GJ, Domann S, Nelson A, Berry A. Modifying the stereochemistry of an enzyme-catalyzed reaction by directed evolution. Proc Natl Acad Sci USA 2003;100:3143–3148. [PubMed: 12626743]

27. Schneider TD, Stephens RM. Sequence logos: a new way to display consensus sequences. Nucleic acids research 1990;18:6097–6100. [PubMed: 2172928]

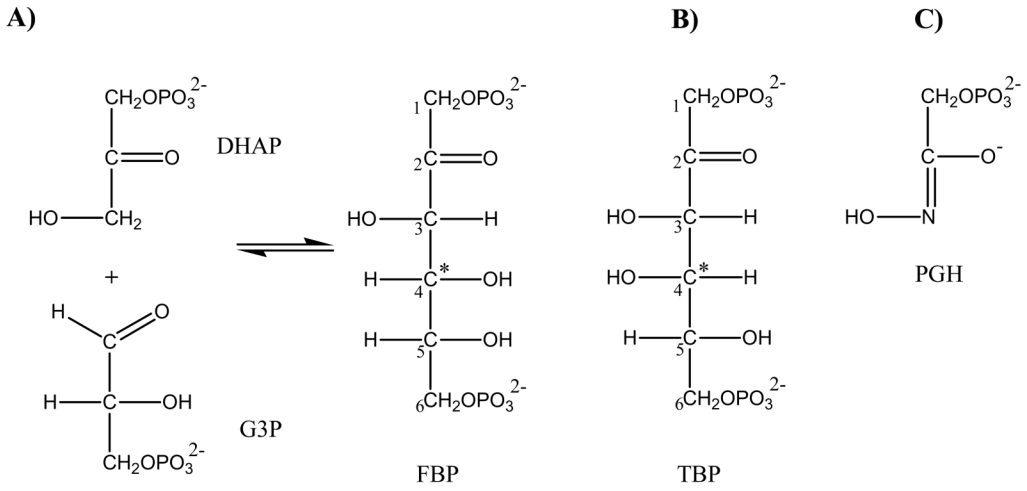

Figure 1.
(A) The reaction catalyzed by fructose-1,6-bisphosphate aldolase (FBPA). (B) D-tagatose-1,6-bisphosphate (TBP), a C(4) hydroxyl epimer of D-fructose-1,6-bisphosphate (FBP). (C) phosphoglycolohydroxamate (PGH), a DHAP ene-diolate transition-state analog.

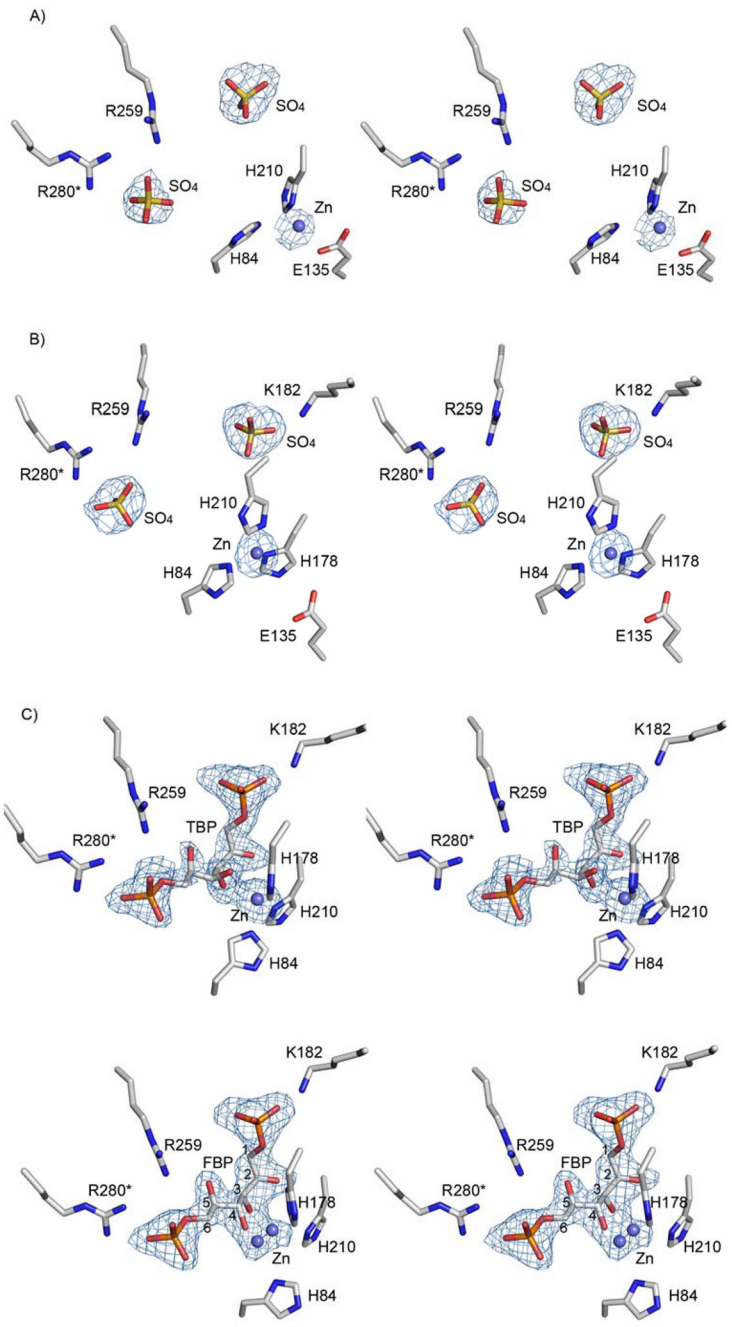

Figure 2.

Stereoscopic view of the electron density map in the vicinity of the active site. Difference Fourier electron density maps with the coefficients $F_o - F_c$ and calculated phases generated omitting the ligands and zinc co-factors from the models. The maps are countered at 3σ level. (A & B) The apo structure contains sulfate ions and each subunit of the dimer exhibits different Zn^{2+} environment. Data resolution: 2.9 Å (C) Bound TBP. Data resolution: 1.8 Å (D) Bound FBP. Data resolution: 2.0 Å

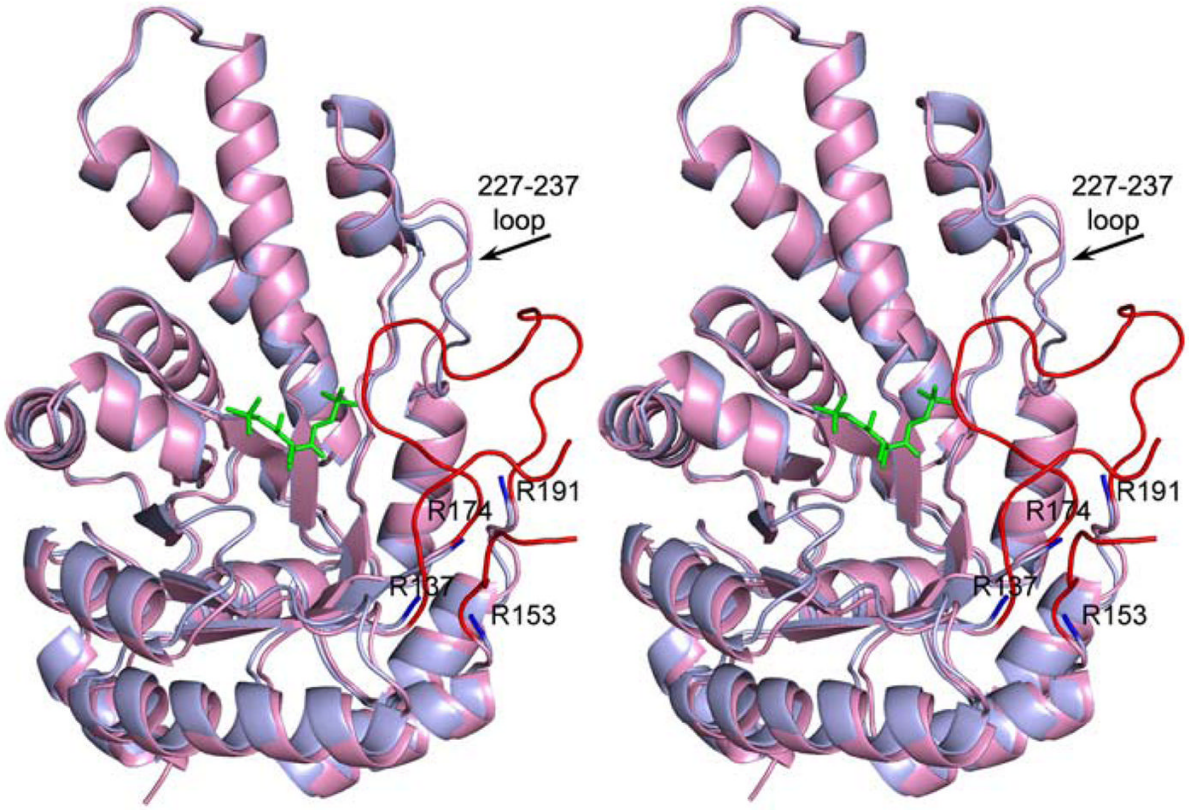

Figure 3.

Stereoscopic representation of *gl*FBPA in the unbound and ligand-bound states. The superposed molecules are depicted in blue (unbound) and pink (bound state) colors where the trace of the polypeptide chain is similar in both structures. The major differences occur in two loop regions: The terminal fragments of the two disordered loops of the apo *gl*FBPA structure are highlighted in blue, and the same loops of the *gl*FBPA/FBP structure are highlighted in red. The FBP is depicted as green stick model.

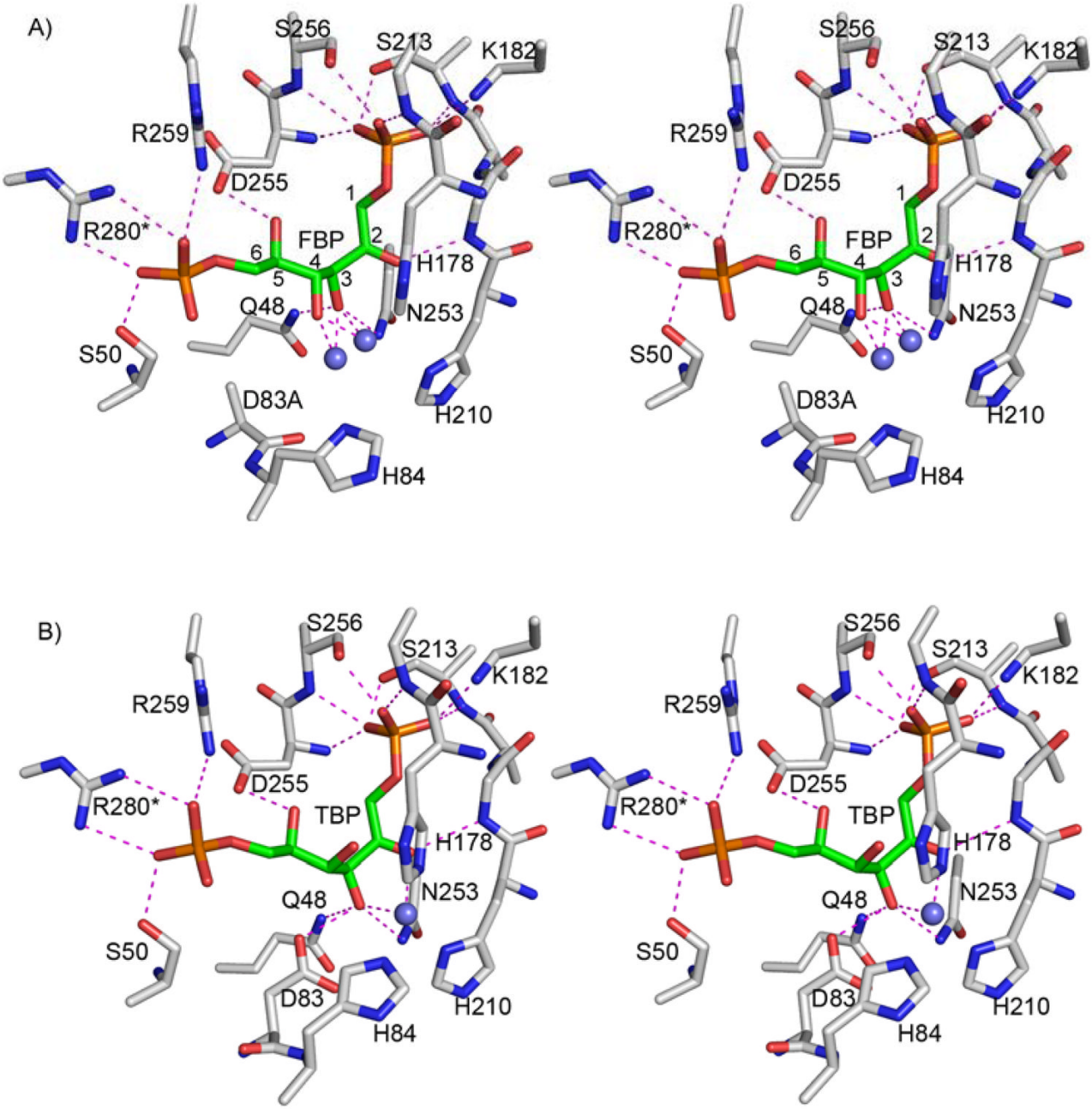

Figure 4.

Binding of FBP (A) and TBP (B) to *gl*FBPA. Stereoscopic view of the environment around the active site. Atomic colors are as follows: oxygen, red; nitrogen, blue; carbon (protein), gray; carbon (ligand), green; phosphor, orange; and zinc, steel blue. Key electrostatic interactions of the ligands are shown in dashed lines.

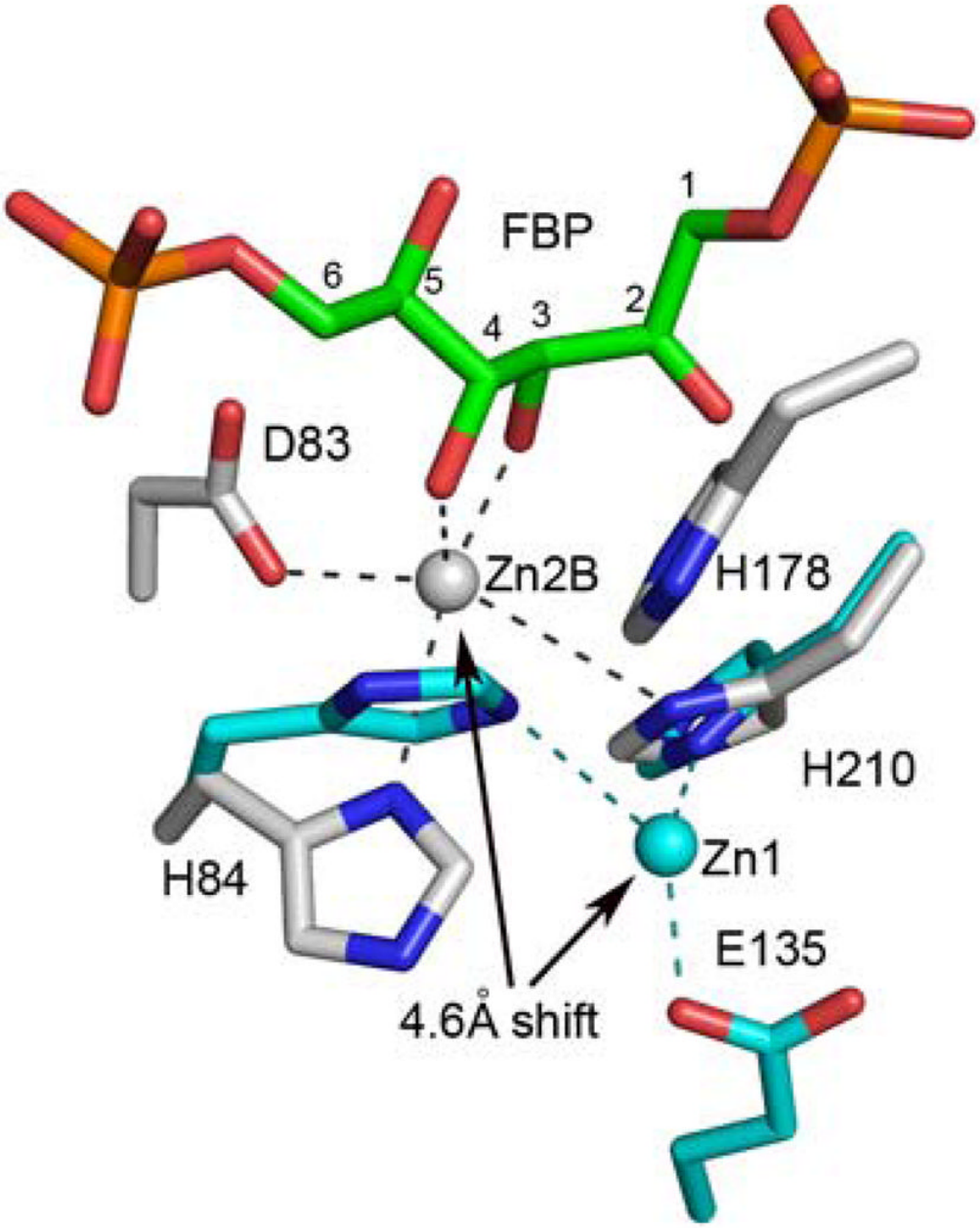

Figure 5.
Local active site conformational transition associated with FBP binding to *gl*FBPA (with a model of Asp83 based on other wild-type *gl*FBPA structures). The Zn^{2+} position shifts by 4.6 Å towards the catalytic Asp83, which changes its coordination so that in the substrate cleavage mode (Zn2B) the Asp83 is coordinated to Zn^{2+}. The Zn^{2+} and carbon atoms of the apo enzyme are colored in cyan. Other atomic colors are the same as in Figure 4. Note that His178 is disordered in the apo structure

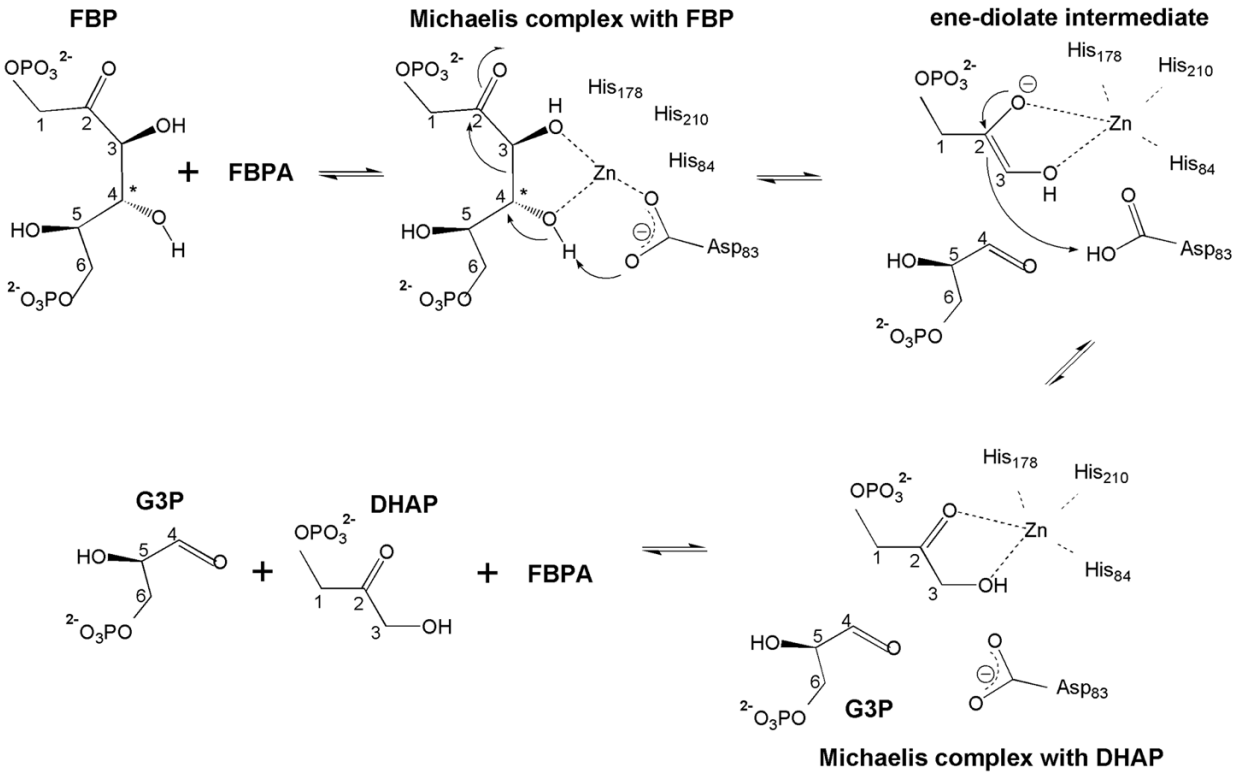

Figure 6.

Proposed catalytic mechanism of class II FBPA. The FBP C(4) position, the chirality of which distinguishes FBP from TBP, is indicated by an asterisk. Carbon numbering from 1 to 6 is maintained also after bond cleavage for clarity.

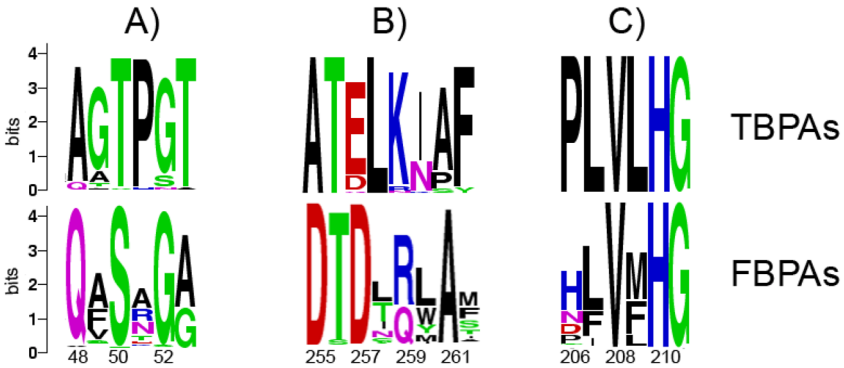

Figure 7.

Sequence logos (27) of multiple sequence alignment for three regions of the FBPA and TBPA subfamilies. The overall height of the stack indicates the level of sequence conservation at each position and the height of symbols within the stack indicates the relative frequency of the particular amino acid at the position. The *gl*FBPA numbering was used and every other amino acid residue is numbered.

Table 1
X-ray data collection and refinement statistics

	wild-type/TBP	D83A/FBP	wild-type
Data collection			
Space group	$P2_12_12_1$	$P2_12_12_1$	$P6_1$
Cell dimension			
a, b, c (Å)	56.3, 67.6, 171.7	56.5, 67.2, 172.2	62.9, 62.9, 318.6
Resolution range (Å)	20–1.8	20–2.0	10–2.9
No. observations	338737	126831	25089
No. unique reflections	57852	41123	13288
Completeness (%)[a]	93.9(62.9)	90.6(50.4)	86.6(98.7)
$I/\sigma(I)$	15.1(1.9)	10.9(2.5)	6.0(2.5)
R_{merge}[b]	0.066(0.342)	0.051(0.257)	0.114(0.250)
Refinement statistics			
No. reflections	57851	41081	12210
No. residues	637	635	592
No. water molecules	578	569	0
No. Zn^{2+}	2	4	2
R_{cryst}/R_{free}[c]	0.199/0.240	0.198/0.254	0.220/0.286
RMS deviation			
Bonds (Å)	0.018	0.014	0.016
Angles (°)	1.7	1.7	1.7

[a] The values in parentheses are for the highest resolution shell

[b] $R_{merge} = \Sigma_{hkl}[(\Sigma_j \mid I_j - < I > \mid)/\Sigma_j \mid I_j \mid]$, for equivalent reflections

[c] $R_{cryst} = \Sigma_{hkl} \mid |F_o| - |F_c| \mid / \Sigma_{hkl} |F_o|$, where F_o and F_c are the observed and calculated structure factors, respectively. R_{free} is computed for 5% of reflections that were randomly selected and omitted from the refinement

Table 2

Metal-ligand interactions in class II FBPAs

Structure	Metal site	Ligands	Distance (Å)	Notes
*gl*FBPA - apo				
molecule A	Zn1	His210 Nδ1	2.0	2.9 Å resolution structure no solvent model incomplete coordination geometry
		His84 Nε2	(3.2)	
		Glu135 Oε1	(3.1)	
		Glu135 Oε2	2.2	
molecule B	Zn2	His210 Nδ1	2.3	as above
		His84 Nε2	2.2	
		His178 Nε2	2.8	
*gl*FBPA/TBP	Zn2	His210 Nδ1	2.3	trigonal bipyramidal
		His84 Nε2	2.4	
		His178 Nε2	2.2	
		TBP C (2)O	2.9	
		TBP C (3)O	2.6	
*gl*FBPA/PGH (pdb:2isw, (10))	Zn2	His210 Nδ1	2.2	trigonal bipyramidal Zn^{2+} is coplanar with the PGH's O-C (2)-N (3)-O
		His84 Nε2	2.1	
		His178 Nε2	2.3	
		PGH C (2)O	2.5	
		PGH N (3)O	2.6	
*gl*FBPA D83A/FBP	Zn2A	His210 Nδ1	2.9	mutually exclusive with Zn2B, highly distorted pentagonal coordination
		His84 Nε2	(3.4)	
		His178 Nε2	(3.1)	
		FBP C (3)O	2.2	
		FBP C(4)O	2.1	
	Zn2B	His210 Nδ1	(3.5)	mutually exclusive with Zn2A; when Asp83 is modeled (Fig. 5), forms highly distorted pentagonal coordination that Includes Asp83; Zn^{2+} is coplanar with the O-C(3)-C(4)-O
		His84 Nε2	(3.0)	
		FBP C(3)O	2.1	
		FBP C(4)O	2.2	
*ec*FBPA - apo				
(pdb:1zen, (4)) tetrahedral	Zn1	His264 Nδ1	2.4	described as distorted
		His110 Nε2	2.6	

Structure	Metal site	Ligands	Distance (Å)	Notes
		His226 Nε2	2.5	
		Glu174 Oε1	2.5	
		Glu174 Oε2	2.8	
	Zn3	His264 Nδ1	2.6	described as distorted tetrahedral
		Lys284 Nζ	2.7	
		Asp109 Oδ1	2.5	
		Glu172 Oε1	2.9	
		Glu172 Oε2	2.5	
(pdb:1dos, (3))	Zn1	His264 Nδ1	2.1	mutually exclusive with Zn2, tetrahedral
		His110 Nε2	2.1	
		His226 Nε2	2.1	
		Glu174 Oε2	2.3	
	Zn2	His264 Nδ1	2.3	mutually exclusive with Zn1, tetrahedral
		His110 Nε2	2.1	
		Wat1 O	2.4	
		Wat2 O	2.3	
*ec*FBPA/PGH (pdb:1b57, (5))	Zn2	His264 Nδ1	1.9	trigonal bipyramidal Zn^{2+} is coplanar with the PGH O-C (2)-N(3)-O
		His110 Nε2	2.1	
		His226 Nε2	1.9	
		PGH C (2)O	2.2	
		PGH N (3)O	2.3	
	Zn4	Glu174 Oε2	2.0	tetragonal
		Glu181 Oε2	1.9	
		Asp144 Oδ2	2.0	
		Wat O	2.1	

[a]The values in parentheses indicate distances that are too large for optimal Zn-ligand coordination, nevertheless, these residues are oriented towards the Zn.

Table 3

Steady-state kinetic parameters for the wild-type and D255A mutant of glFBPA

Substrate	Parameter	Wild-type	D255A
FBP	k_{cat} (s^{-1})	3.55 ± 0.05	0.63 ± 0.03
	K_m (μM)	1.7 ± 0.1	16± 2
	k_{cat}/K_m($M^{-1}s^{-1}$)	2×10^6	4×10^4
TBP	k_{cat} (s^{-1})	-[a]	0.003 ± 0.0002[a]
	K_m (μM)	-	37 ± 7
	k_{cat}/K_m($M^{-1}s^{-1}$)	-	80

[a] The limit of detection of TBPA activity is 1×10^{-5} S^{-1}. The observed k_{cat} for the D255A mutant is 2 orders of magnitude higher.